Front. Energy 2025, 19(6): 925–938
https://doi.org/10.1007/s11708-025-1003-7

RESEARCH ARTICLE

Experimental study on early flame dynamics in an optically accessible hydrogen-fueled spark ignition engine

Hao Shi (✉)[1], Cooper Welch[1], Jannick Erhard[1], Pedro Ye[1], Hongchao Chu[2], Andreas Dreizler[1], Benjamin Böhm[1]

1 Department of Mechanical Engineering, Reactive Flows and Diagnostics, Technical University of Darmstadt, Otto-Berndt-Str. 3, 64287 Darmstadt, Germany
2 Institute for Combustion Technology, RWTH Aachen University, 52056 Aachen, Germany

Abstract Hydrogen, with its carbon-free composition and the availability of abundant renewable energy sources for its production, holds significant promise as a fuel for internal combustion engines (ICEs). Its wide flammability limits and high flame speeds enable ultra-lean combustion, which is a promising strategy for reducing NO_x emissions and improving thermal efficiency. However, lean hydrogen-air flames, characterized by low Lewis numbers, experience thermo-diffusive instabilities that can significantly influence flame propagation and emissions. To address this challenge, it is crucial to gain a deep understanding of the fundamental flame dynamics of hydrogen-fueled engines. This study uses high-speed planar SO_2-LIF to investigate the evolutions of the early flame kernels in hydrogen and methane flames, and analyze the intricate interplay between flame characteristics, such as flame curvature, the gradients of SO_2-LIF intensity, tortuosity of flame boundary, the equivalent flame speed, and the turbulent flow field. Differential diffusion effects are particularly pronounced in H_2 flames, resulting in more significant flame wrinkling. In contrast, CH_4 flames, while exhibiting smoother flame boundaries, are more sensitive to turbulence, resulting in increased wrinkling, especially under stronger turbulence conditions. The higher correlation between curvature and gradient of H_2 flames indicates enhanced reactivity at the flame troughs, leading to faster flame propagation. However, increased turbulence can mitigate these effects. Hydrogen flames consistently exhibit higher equivalent flame speeds due to their higher thermo-diffusivity, and both hydrogen and methane flames accelerate under high turbulence conditions. These findings provide valuable insights into the distinct flame behaviors of hydrogen and methane, highlighting the importance of understanding the interactions between thermo-diffusive effects and turbulence in hydrogen-fueled engine combustion.

Keywords H_2 internal combustion engines (ICEs), optical diagnostics, early flame dynamics, thermo-diffusive instability, flame morphology

1 Introduction

The need to transition to a low-carbon economy is urgent due to the increasing impact of global warming. Hydrogen, as a carbon-free fuel, has significant potential to reduce greenhouse gas emissions and is considered crucial for future energy systems [1], including hydrogen-fueled internal combustion engines (H_2-ICE) [2]. Hydrogen's broad flammability limits allow combustion under highly dilute conditions, reducing NO_x emissions while maintaining high thermal efficiency [3]. However, lean hydrogen flames are prone to thermo-diffusive instabilities that affect flame dynamics and heat release rates, leading to an increase in the turbulent flame speed [4–7] These instabilities are challenging to model accurately with current combustion frameworks [8,9]. Compared to hydrocarbon fuels like methane, hydrogen combustion presents unique challenges due to its higher diffusivity, leading to significant differential diffusion effects [10]. This can influence early flame kernel development, which is known to contribute to cycle-to-cycle variations (CCVs). The early flame kernel development is influenced by turbulence-flame interactions and thermo-diffusive instabilities, which alter flame morphology in time and space, complicating the

Received Dec. 21, 2024; accepted Mar. 12, 2025; online Apr. 15, 2025
Correspondence: Hao Shi, hao.shi@rsm.tu-darmstadt.de

prediction and control of the combustion in hydrogen engines [4,11]. Understanding the early flame structures in H_2-ICEs is thus crucial for elucidating the underlying hydrogen combustion physics and developing accurate and predictive combustion models [12].

Previous studies have highlighted the pronounced impacts of the thermo-diffusive instabilities on hydrogen combustion. Early work by Haibel and Mayinger [13] observed elongated flame folds in lean hydrogen combustion, with flame pockets detaching due to strong thermo-diffusive effects, and they attributed these structures to differential diffusion effects. Wu et al. [14] reported that lean hydrogen flames led to higher distortions and increased turbulent burning velocities due to differential diffusion effects. Berger et al. [8] numerically observed similar results, noting that thermo-diffusive instabilities can increase flame speeds up to four times the unstretched laminar burning velocity in lean hydrogen/air mixtures at ambient conditions. Moreover, Chu et al. [4] conducted direct numerical simulations of lean hydrogen flame kernels under engine conditions. Significant effects of thermo-diffusive instabilities on the early flame kernel development were observed. However, these trends have not yet been reported in experiments, especially under engine operating conditions.

Understanding hydrogen flame dynamics and turbulence-flame interactions, particularly in the presence of thermo-diffusive and hydrodynamic instabilities, requires comprehensive experimental data obtained through optical diagnostics. However, such data for hydrogen combustion in modern engines are currently limited. For instance, Salazar and Kaiser [15] used high-speed Schlieren imaging to visualize hydrogen flame propagation, observing that high in-cylinder tumble significantly influenced the convection and stretching of the hydrogen flame across most cycles. Aleiferis and Rosati [16] employed OH-LIF to study detailed features of the hydrogen flame front, revealing distorted macro-scale shapes and frequent small-scale wrinkling, particularly around ϕ = 0.50. Peñaranda et al. [17] conducted measurements in an optically accessible single-cylinder port fuel injection spark-ignition engine, comparing methane and various CH_4/H_2 mixtures. They found that higher hydrogen concentrations resulted in more pronounced flame front wrinkling and enhanced flame speed. The spatial resolution of these measurements has not yet been sufficient to resolve the flame front on the level of the cell structures of thermos-diffusive instabilities for engine relevant conditions. However, this is a prerequisite for studying the effect of thermo-diffusive instabilities on flame propagation and for validating and improving current simulation models.

This study aims to fill this gap by providing high resolution data on the flame front within an optically accessible engine to investigate the effects of thermo-diffusive instabilities on the development of the early flame kernel for lean H_2/air mixtures. Additionally, it seeks to provide experimental validation data for hydrogen combustion in H_2-ICEs. To achieve this, the early hydrogen flame was visualized within the central tumble plane using high-speed planar laser-induced fluorescence of sulfur dioxide (SO_2-PLIF) and compared against methane—a reference fuel with near-unity Lewis number ($Le \approx 1$)—isolating the differential diffusion effects unique to hydrogen. SO_2-PLIF was chosen due to its significant increase in fluorescence intensity with rising temperature, resulting in a sharp gradient at the reaction zone [18]. Honza et al. [19] showed that the SO_2 LIF signal closely tracks the temperature rise within the reaction zone, making it a reliable flame marker. In this work, flame front and curvature statistics for different fuels (H_2 vs. CH_4) are compared and discussed. The crank-angle-resolved analysis of flame curvature, tortuosity, and gradients provides unprecedented insights into how instabilities modulate flame propagation, offering experimental validation for next-generation combustion models. The influence of turbulence on the flame is examined based on a statistical analysis of two different engine operating conditions with a load variation to elucidate the effects of thermo-diffusive instabilities on flame development.

2 Experimental setup and methodology

2.1 Optical engine

The experiments were conducted on an AVL single-cylinder optical spark-ignition (SI) engine (Fig. 1), featuring a twin-cam, overhead-valve pent-roof cylinder head. This engine has a compression ratio of 8.7, with both bore and stroke measuring 86 mm. The seamless alignment of the quartz-glass cylinder liner (thickness: 20 mm, height: 55 mm) with the pent-roof cylinder head provides extensive optical access to the combustion chamber. Further engine specifications are detailed in Baum et al. [20].

This study focused on two fuels, H_2 and CH_4, which were introduced upstream of the intake valves to ensure a homogeneous air-fuel mixture. Stoichiometric CH_4/air mixtures were used as a baseline, and the equivalence ratio (λ) of the H_2/air mixtures was varied until the 50% mass fraction burned occurred at 8°CA after the top dead center from the same ignition timing. To facilitate direct comparisons between hydrogen and methane combustion, the engine operating conditions, including engine speed, intake pressure, and ignition timing, were maintained identically for both fuels. This ensured that ignition and early flame kernel development occurred for both fuels under comparable thermodynamic and turbulent flow conditions. The operating conditions (OC) B and A are listed in Table 1 to provide a detailed overview. The

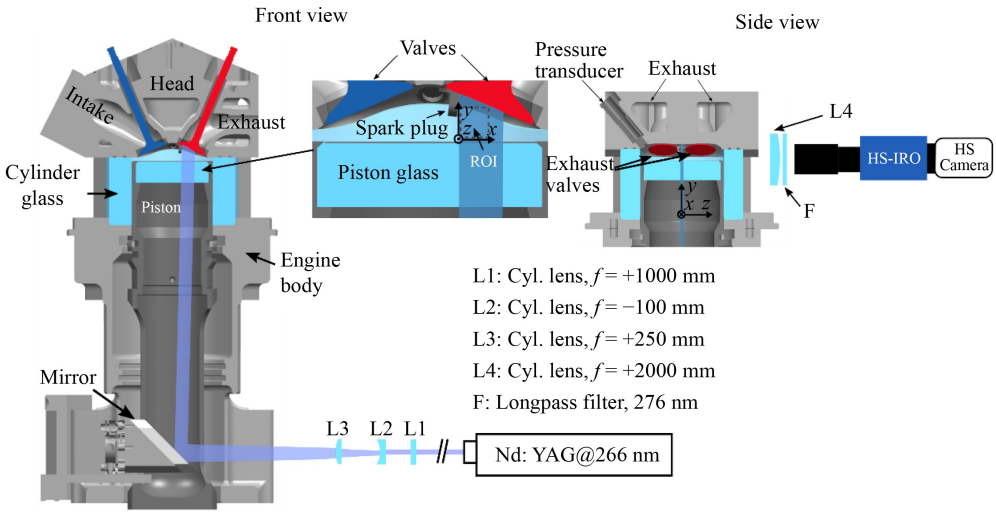

Fig. 1 Schematic of the experimental setup.

Table 1 Engine operating conditions

OC	N/(r·min)	P_{in}/bar	Fuel	λ	Le_{eff}	t_{ign}/°CA	P_{ign}/bar	T_{ign}/K	ρ_{ign}/(kg·m^{-3})	ν_{ign}/(m^2·s^{-1})×10^{-5}
B	800	0.400	H_2	2.36	0.377	−36.6	2.511	532.6	1.485	1.665
B	800	0.403	CH_4	1.02	1.019	−36.6	2.482	543.4	1.724	1.477
A	800	0.951	H_2	2.53	0.373	−16.6	10.99	635.7	5.475	0.517
A	800	0.952	CH_4	1.00	1.014	−16.6	10.88	650.5	6.460	0.440

effective Lewis number for the different OCs, Le_{eff}, was calculated based on the thermal and mass diffusivities of the gas mixtures, following the methodology outlined in Welch et al. [21]. Figure 2 shows the mean and standard deviation of pressure for H_2 and CH_4 combustion under Conditions B and A. The in-cylinder gas temperature at ignition timing (T_{ign}) was calculated based on the intake pressure (P_0), intake temperature (T_0), and in-cylinder pressure at ignition timing (P_{ign}), assuming an isentropic compression process between intake valve closure and ignition. This is supported by measurements of the gas temperature in the cylinder [22], which show that the assumption of an isentropic compression holds until top dead center, while the temperature deviates more and more during expansion [22]. Although previous PIV experiments conducted on this optical engine [23] showed no significant change in the flow field velocities, neither for the mean nor for the fluctuations, between B and A, the increased intake pressure results in higher density (ρ) and lower kinematic viscosity (ν) of the mixture, as shown in Table 1. The reduced kinematic viscosity facilitates the formation of smaller vortex structures, thereby promoting turbulence within the cylinder. More details are described in Welch et al. [21].

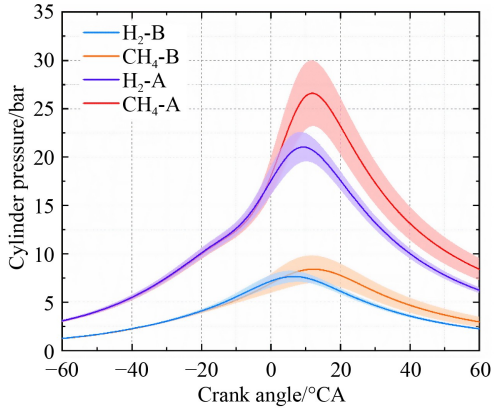

Fig. 2 Mean (solid line) and standard deviation (shaded area) of the in-cylinder pressure for B and A.

2.2 SO_2-PLIF

The optical setup for the SO_2-PLIF experiment is shown in Fig. 1. The SO_2 tracer was introduced into the intake air at concentrations of 1.3 vol% and 0.6l vol% for Conditions B and A, respectively. Excitation was achieved at a wavelength of 266 nm using the fourth harmonic generation of a high-speed Nd:YAG laser (Edgewave, INNOSLAB), operating at a repetition rate of 8 kHz and a pulse energy of 520 μJ. The fluorescence signal was captured using a high-speed image intensifier (HS-IRO, LaVision) paired with a high-speed camera (Phantom v2640, Vision Research). Astigmatism induced by the glass liner was mitigated using a correction lens, and a long-pass filter was employed to protect the intensifier from laser reflections.

The detection system covered a region of interest located on the exhaust side, near the spark plug, to observe early flame development, with an optical resolution of 215 μm (4.70 LP/mm). Planar LIF images were captured with a crank angle resolution of 0.6 °CA (8 kHz), starting 2 °CA before ignition to obtain background images. A programmable timer unit (PTU 11, LaVision GmbH) and DaVis 10.2 software (LaVision GmbH) were used to synchronize the LIF measurements with the engine.

To ensure consistency across measurements, the engine was operated according to a work-rest protocol: 300 fired cycles for warm-up, followed by 150 unfired cycles, and then 300 fired cycles for data acquisition. The subsequent data analysis was performed using the last 100 cycles of each measurement run. Further details of the setup can be found in Welch et al. [21].

2.3 Image post-processing

The post-processing procedure for the PLIF images is illustrated in Fig. 3. Initially, the raw images were dewarped and transformed into real-world coordinates using a 3rd-order polynomial fit. A geometric mask was then applied to the dewarped images (Fig. 3(a)) to exclude reflective objects, such as the spark plug and piston. To correct the laser profile, each image was normalized by the spatially averaged intensity along the laser sheet, which was calculated from an image acquired during the late-combustion phase. This normalization yielded corrected images (Fig. 3(b)).

Next, background subtraction was performed using the average background noise level, determined from images taken before ignition. To mitigate the influence of wall effects, flame regions near the cylinder head, walls, and piston top were excluded. The resulting images (Fig. 3(c)) were then denoised and smoothed through a series of filtering steps: median filtering, bilateral filtering, and nonlinear diffusion (NLD) filtering, resulting in the final processed images (Fig. 3(f)).

Before binarization, each filtered image (Fig. 3(f)) was normalized to its maximum intensity. Otsu's method was employed to determine a single threshold value for binarizing each image. Flame boundaries were extracted from the binarized images (Fig. 3(g)) using a hybrid filtered Canny edge detection algorithm.

To quantify the morphological variations of flame fronts (Fig. 3(h)) and the evolution of flame kernels, several parameters were utilized to analyze the flame characteristics. The local curvature (Fig. 3(i)) was calculated from the flame front coordinates (x, y) using Eq. (1) in Gashi et al. [24]

$$k = \frac{x'y'' - y'x''}{(x'^2 + y'^2)^{3/2}}, \tag{1}$$

where k is used to characterize the flame troughs ($k > 0$) and the flame cusps ($k < 0$), and a detailed explanation can be found in Shi et al. [25]. The curvature value at

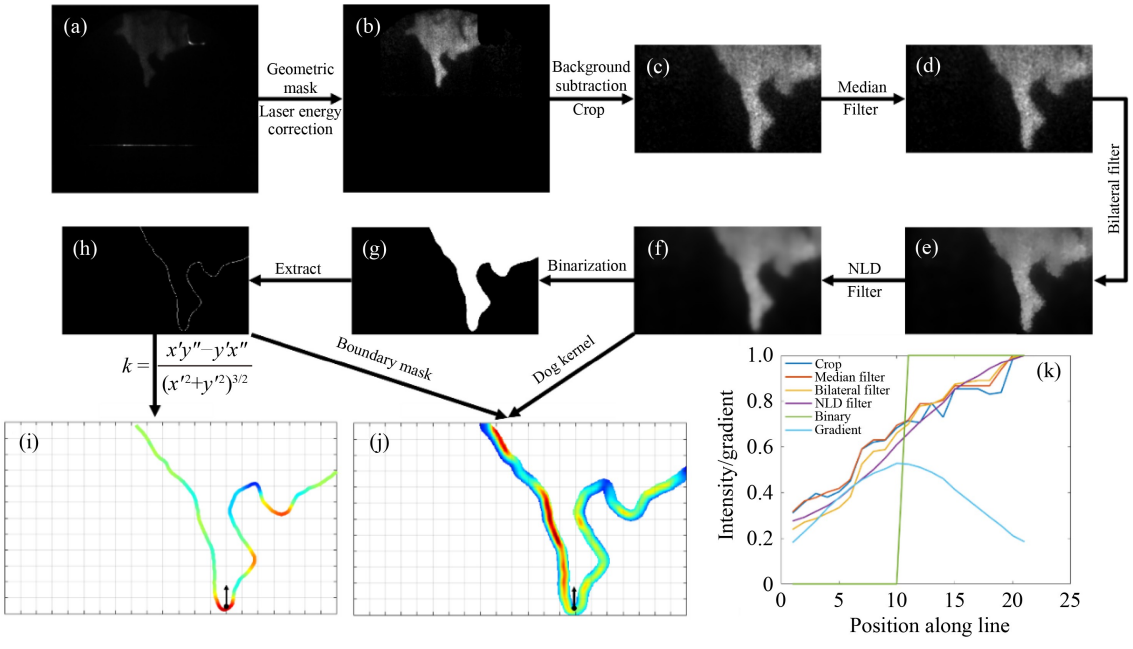

Fig. 3 Image post-processing procedures.

(a) Raw image after dewarping; (b) image after geometric mask and laser energy correction; (c) cropped and background-subtracted image; (d) denoised image using median filtering; (e) denoised image using a bilateral filter; (f) denoised image using a NLD filter; (g) binarized image; (h) extracted flame front; (i) flame curvature; (j) flame gradient maps; (k) 1D flame intensity/gradient profiles across the flame front (the measurement location is indicated by the arrows in (i) and (j)).

each pixel along the flame boundary was evaluated based on the positions (x, y) of five adjacent points along the flame front centered at this pixel.

Based on the filtered image (Fig. 3(f)), the two-dimensional flame gradients, derived from SO_2-PLIF intensity, were computed using a derivative of the Gaussian (DoG) kernel with a standard deviation of 2 pixels [26]. The resulting gradient maps (Fig. 3(j)) were normalized by their maximum values to compensate for variations in laser energy. A geometric mask, with a thickness of 8 pixels, was applied to highlight the gradient near the flame boundary. Figure 3(k) presents 1D profiles of flame intensity and gradient along a vertical line intersecting the primary flame trough (indicated by the arrow in Figs. 3(i) and 3(j)). These profiles demonstrate the efficacy of the combined filtering approach in smoothing the flame intensity near the front and accurately identifying the flame boundary location. The peak locations of both the intensity and gradient profiles coincide closely with the flame boundary, confirming the robustness of the post-processing procedure.

To focus on the free propagation and dynamic behavior of early flame kernels, the initial frames before flame kernel emergence and late frames after flame impingement on the end walls were removed from the analysis. The first and last valid frames were designated A0 and A100, respectively. Due to variations in flame speed across different fuels and conditions, differences in flame topologies and dynamics were observed even at identical time instances after ignition. To facilitate comparisons among the different cases and analyze curvature characteristics and flame dynamics during early flame propagation, four stages of flame growth, defined by area percentages (20%, 40%, 60%, 80%), were used. The actual area ratio, A_X, was defined as

$$A_X = \frac{FA - FA_0}{FA_{100} - FA_0}, \tag{2}$$

where FA denotes the actual flame area, FA_0 indicates the flame area at A_0, and FA_{100} represents the flame area at A_{100}.

The tortuosity of the flame boundary is quantified by integrating the square of the derivative of curvature, divided by the length of the curve, as shown in Eq. (3) in Grisan et al. [27]

$$\tau = \frac{\int_{C_1}^{C_2} k'(C)^2 \mathrm{d}C}{L}, \tag{3}$$

where C denotes the flame contour, $k(C)$ is the local curvature, and L is the length of the flame contour.

Moreover, the equivalent flame speed is calculated by Eq. (4)

$$\vartheta_e = \frac{\mathrm{d}r_s(t)}{\mathrm{d}t}, \tag{4}$$

where ϑ_e is the equivalent flame speed, and $r_s(t)$ is the instantaneous flame radius corresponding to the equivalent flame surface area $A(t)$, which is calculated by Eq. (5)

$$r_s(t) = \sqrt{A(t)/\pi}. \tag{5}$$

3 Results and discussion

3.1 Flame contours and curvatures

Selected cycles for the four investigated operating conditions shown in Fig. 4 give an impression of the flame morphologies. The cycle with the largest absolute curvature was selected from each condition (H_2-B, CH_4-B, H_2-A, CH_4-A) for further analysis. The flame contours and curvatures along the flame at four distinct combustion phases (A20, A40, A60, A80) are shown. Additionally, the tortuosity (τ) of the flame boundary is indicated for each combustion phase in each subplot.

For the hydrogen flame under Condition B, the early stage (A20) exhibits pronounced flame troughs (X = 11.5 mm, Y = 5.3 mm) and cusps (X = 12.5 mm, Y = 4.2 mm). As the flame propagates (A20 to A40), the flame trough at X = 11 mm accelerates, and the distances between the flame trough and cusp increase. The emergence of a second flame trough at A40 highlights the dynamic nature of turbulent hydrogen flame propagation. Between A40 and A60, the flame boundary becomes more convoluted, as evidenced by the increased tortuosity. The leading flame troughs accelerate leading to a larger flame area. Meanwhile, an additional flame trough is formed at the side of the primary flame leading edge. Between A60 and A80, the trough regions exhibit substantially faster propagation velocities compared to the flame cusps, resulting in a marked expansion of the flame area. In contrast, the selected representative methane flame (CH_4-B) exhibits random fluctuations in trough/cusp structures, with less pronounced variations in the velocities of the leading trough. The flame tortuosity of CH_4-B is lower than that of the H_2-B flame across the investigated combustion phases.

Upon transitioning from Condition B to Condition A, both H_2/air and CH_4/air flames exhibited increased wrinkling, higher curvatures, and a more pronounced appearance of flame trough/cusp structures along the flame fronts. The increased randomness in wrinkle formation suggests a more dominant role of turbulence under these conditions. This phenomenon underscores the exacerbation of flame wrinkling under elevated pressure and the associated intensified turbulence, primarily attributed to the presence of smaller eddies because the dissipation of turbulence shifts toward smaller scales due to the reduced kinematic viscosity. Moreover, the

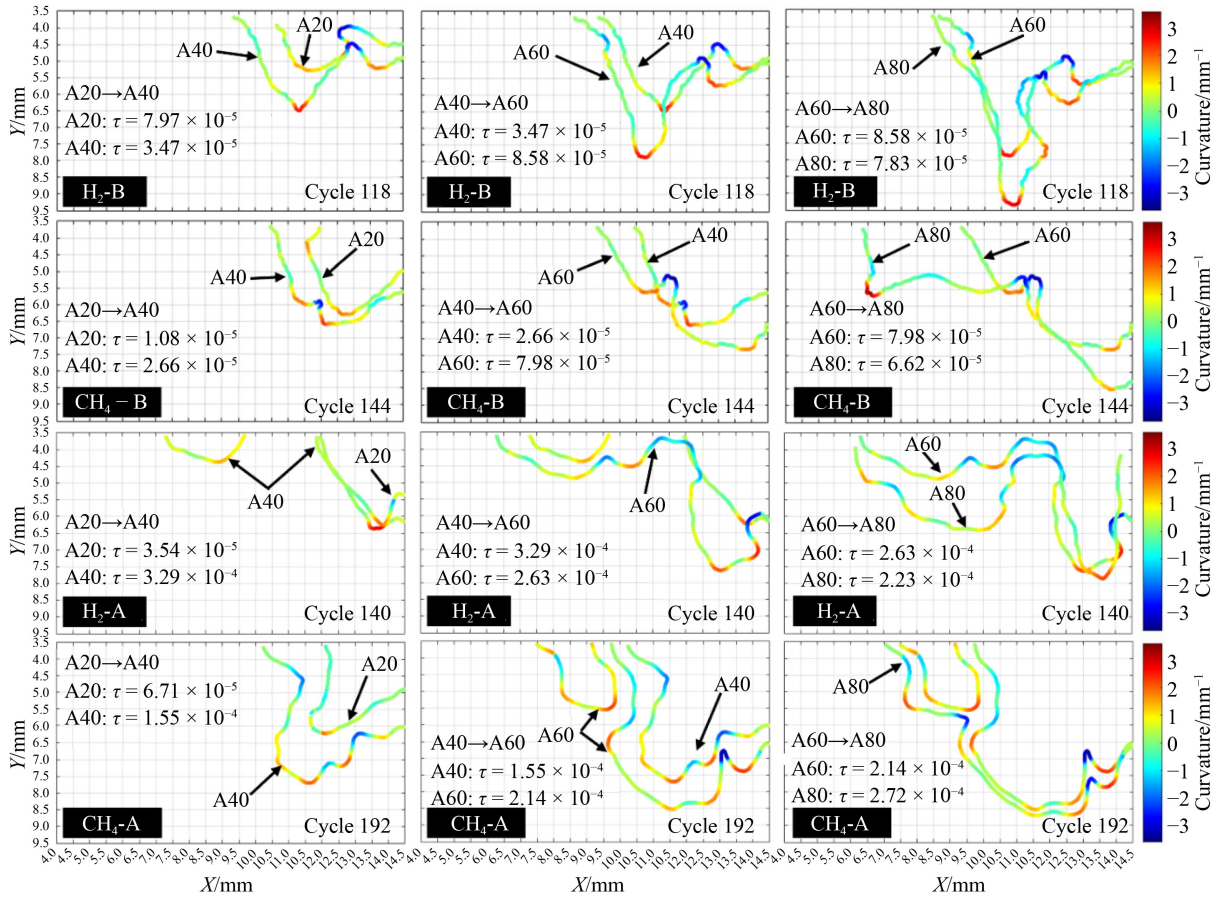

Fig. 4 Evolution of flame morphology and curvature during different combustion phases (A20, A40, A60, A80) for hydrogen and methane flames under Conditions B and A (the lower left corner of each subplot indicating the fuel types and conditions, and the lower right corner denoting the cycle index, the overlaid text describing the transitions between combustion phases and the evolution of flame boundary tortuosity (τ)).

difference in tortuosity between the H_2 and CH_4 cycle has decreased for operating point A, suggesting that the previously observed enhanced flame wrinkling of H_2 due to thermo-diffusive instabilities may be suppressed by increased turbulence.

To investigate this observation, a statistical analysis of the flame curvature was conducted for all recorded cycles in Fig. 5 where the two operating conditions for H_2 and CH_4 are shown for the phases A20 to A80. The resulting distributions are all skewed toward positive values, which is particularly pronounced at A20, but can still be clearly observed at A80. This is due to the ignition by the spark plasma, which initially forms a nearly spherical flame kernel, which is positively curved. This begins to wrinkle over time by the turbulent flow field and, in the case of H_2, also by the thermo-diffusive instabilities. The influence of the higher turbulence for Case A can be seen in a broader distribution, in which the wings are more pronounced, especially for negative curvatures. A similar, but much weaker effect can be observed between H_2 and CH_4. For H_2, the distributions show a slightly higher probability of negative curvatures. This difference increases from A20 to A40 and can be attributed to the effect of the differential diffusion of H_2, which is characterized by an effective Lewis number of 0.37 for the lean conditions studied. This leads to another mechanism that wrinkles the flame in addition to turbulence. The steep gradients at the flame lead to a local stratification of the mixture, which, although initially homogeneously distributed, leads to local lambda variations [28]. By locally enriching the mixture in front of the flame troughs ($\phi_{local} > \phi_{global}$) and depleting it in the cusps ($\phi_{local} < \phi_{global}$), the flame speed varies along the flame front, causing additional wrinkling. Since this effect requires time to evolve, an increase in flame wrinkling is expected as time progresses. However, for A60 and A80, this difference between the negative curvatures for H_2 and CH_4 decreases again. This can be attributed to the interaction of the flame with the piston surface where flame-wall interactions start to appear beyond A80. Therefore, it is expected that the upward-moving piston, coupled with its resultant flow field changes, will influence flame propagation already at an earlier time [29].

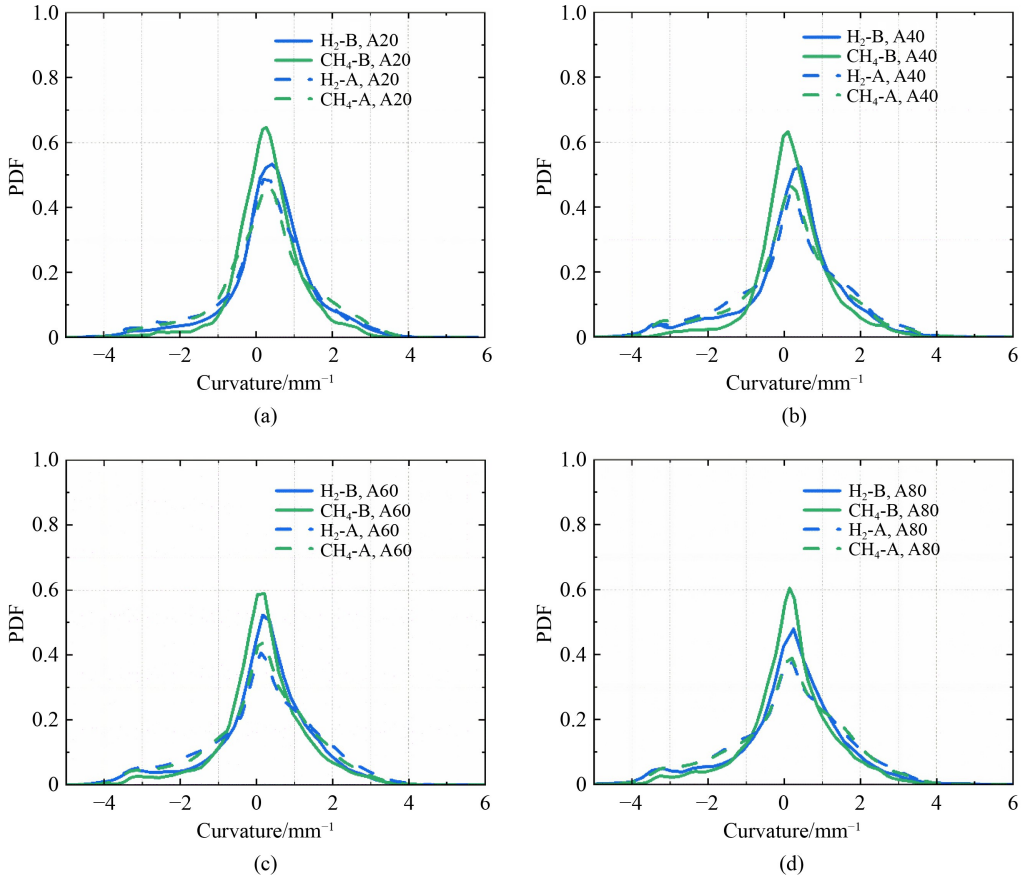

Fig. 5 Flame curvature PDFs for hydrogen and methane flames at various conditions and combustion phases (Conditions A and B; A20–A80).

(a) A20; (b) A40; (c) A60; (d) A80.

3.2 Correlations between flame curvatures and gradients

The analysis of flame curvatures and the gradients of SO_2-PLIF intensity provides valuable insights into the local flame dynamics and its interaction with turbulent eddies. Hydrogen flames, influenced by differential diffusion, exhibit a wider distribution of flame gradients. This finding is consistent with the theoretical predictions by Chu et al. [4], who suggested that the flame speed in hydrogen-enriched mixtures is significantly influenced by the local curvature due to the low effective Lewis number of hydrogen.

This section investigates the disparities in the distributions of flame curvatures and intensity gradients along the flame fronts of hydrogen and methane flames under both operating conditions. The selection of individual cycles with similar flame curvature distributions under Conditions B and A allows for a direct comparison of the flame characteristics. As illustrated in the upper row of Fig. 6(a), the hydrogen and methane flames at A80 from the selected cycles exhibit similar ranges of curvature distribution, despite their distinctly different flame morphologies. The curvatures of the CH_4 flame are more concentrated at zero, suggesting a prevalence of flat flame regions. In contrast, the hydrogen flame demonstrates a higher frequency of nonzero curvatures, indicative of a more wrinkled flame front. This observation supports the idea that the lower effective Lewis number of hydrogen leads to an increased generation of flame curvatures during propagation [30].

The flame gradients of the hydrogen flame also display a wider distribution range compared to the methane flame, with a higher peak PDF, indicating steeper gradients. This observation is further supported by the calculated correlation coefficient (R) between flame curvatures and gradients, which is enhanced significantly by comparing the hydrogen flame (0.52) and the methane flame (0.31). The increased correlation underscores the stronger influence of flame curvature on the local flame gradients in hydrogen flames, suggesting that regions of high curvature coincide with areas of high heat release rate [31] and fuel concentration [32]. The higher gradients in hydrogen flames signify a steeper increase in reaction rates at the flame front, particularly in regions of high curvature, where the local flame speed can exceed the unstretched laminar flame speed by a considerable margin.

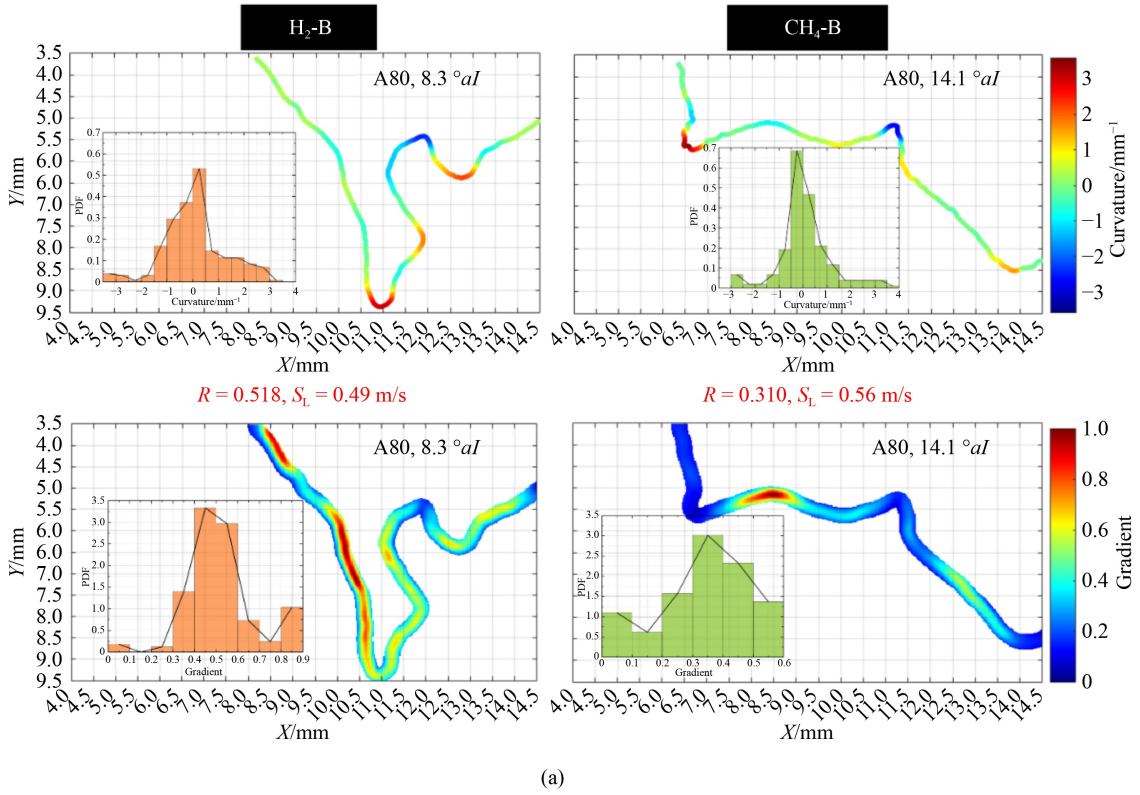

(a)

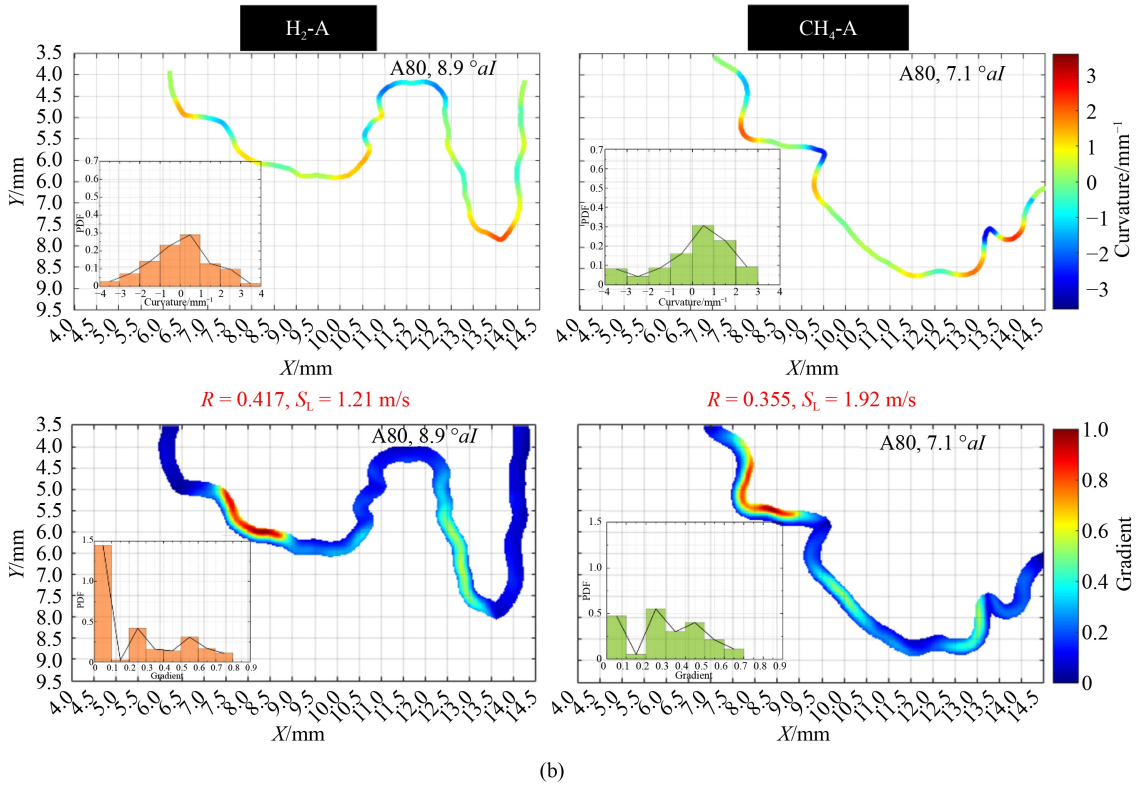

(b)

Fig. 6 Comparative study of flame curvatures and gradients of hydrogen and methane flames (histograms indicating the PDF distributions of flame curvatures and gradients while red texts indicating the correlations (R) between flame curvatures and gradients, and laminar flame speeds (S_L).)

(a) Condition B (H_2 flame: cycle 118; CH_4 flame: cycle 144); (b) Condition A (H_2 flame: cycle 140; CH_4 flame: cycle 192)

Although the unstretched laminar flame speed, calculated using Cantera with the kinetic mechanisms GRI-MECH 3.0 [33–35], reveals that the lean hydrogen flame has a lower speed than the methane flame at the same combustion phase, the practical flame propagation speed of hydrogen flames surpasses that of methane flames, as evidenced by the PDFs of 2D flame area distributions at identical crank angles after ignition (Fig. 7(a)). This discrepancy implies that the differential diffusion and thermo-diffusivity inherent in hydrogen flames may enhance flame propagation, as supported by the enhanced flame wrinkling and tortuosity observed in Fig. 4.

Considering Case A (Fig. 6(b)), the correlation between flame curvatures and gradients for hydrogen flames decreases (0.42), while it increases for methane flames (0.36). This observation aligns with the findings of Shi et al. [28], who employed simultaneous 1D Raman/Rayleigh scattering techniques to demonstrate that local equivalence ratio profiles become flatter under strong turbulence conditions, indicating the dominance of turbulent transport over molecular diffusion. Furthermore, the flame propagation speeds of hydrogen and methane flames become more similar, as presented in Fig. 7(b), even though the theoretical laminar flame speed of

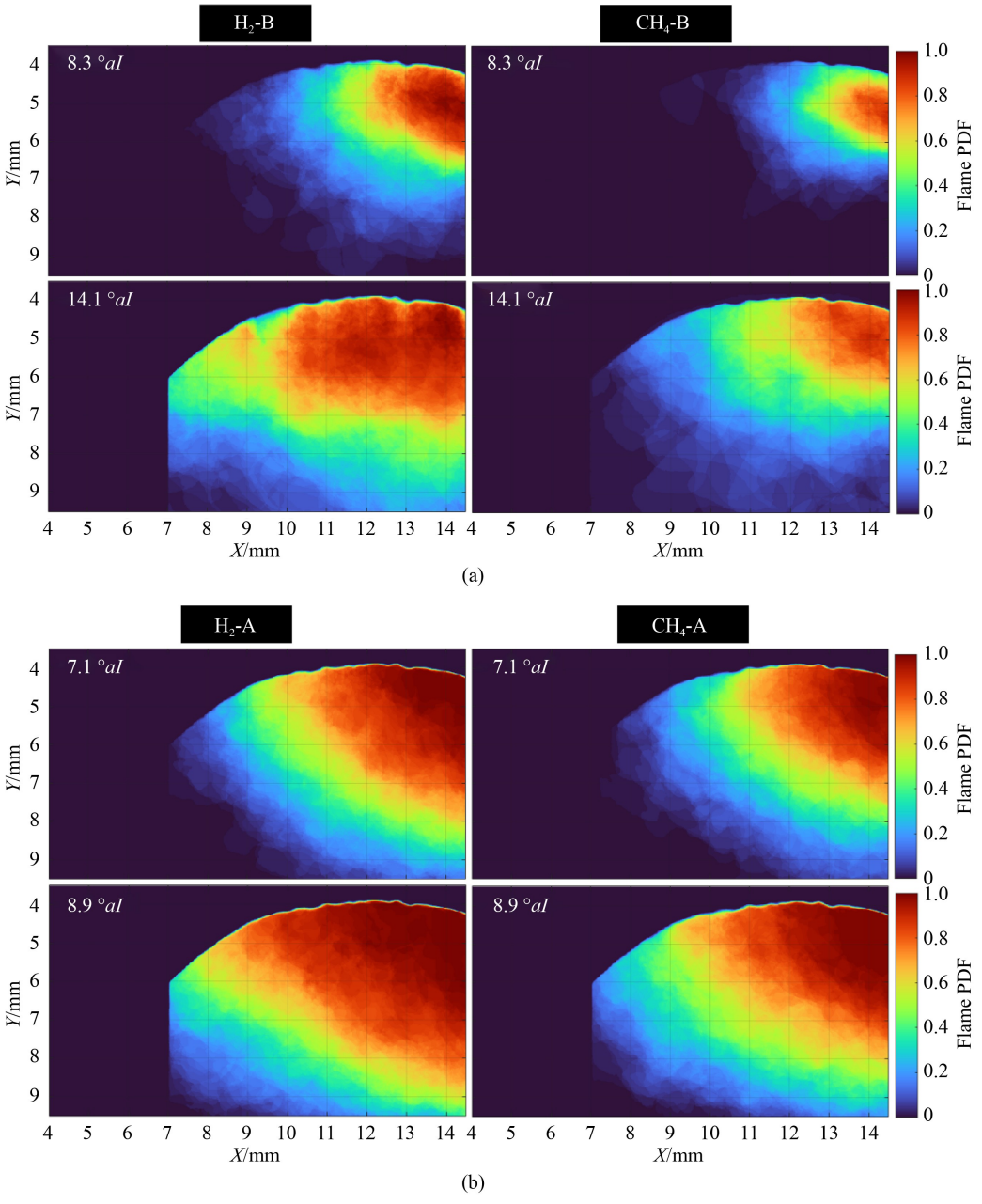

Fig. 7 Flame PDFs of hydrogen and methane flames at the same crank angles after ignition. (a) Condition B; (b) Condition A.

methane flame (1.92 m/s) is 1.58 times higher than that of hydrogen (1.21 m/s). This suggests that the influence of thermos-diffusive instabilities on lean hydrogen flames diminishes as turbulence increases.

The correlation analysis in Fig. 8 provides a quantitative assessment of the relationship between flame curvatures and gradients across all combustion cycles for various combustion phases under Conditions B and A. This detailed statistical evaluation supports the understanding of the underlying mechanisms governing flame propagation in hydrogen and methane flames, underscoring the dynamic interplay between flame curvature and the local flame gradients. The higher correlation coefficients for hydrogen flames, especially under Condition B, imply a stronger coupling between the geometric properties of the hydrogen flame and its reactive characteristics. These results are in line with the findings of Day et al. [36], who observed that the local flame speed in lean hydrogen-air flames is highly sensitive to the flame's curvature, a phenomenon exacerbated by thermo-diffusive instabilities.

Under Condition B, the mean correlation coefficients for hydrogen flames are nearly three times higher than those of methane flames, highlighting the strong influence of curvature on flame gradients for hydrogen. This enhanced correlation suggests that hydrogen flames exhibit a richer fuel concentration at the flame troughs, where curvatures are high. This leads to a localized increase in reaction rates and an acceleration of flame propagation. The higher correlation between curvatures and gradients in hydrogen flames indicates a more vigorous response to differential diffusion effects, which are more significant for hydrogen due to its lower effective Lewis number. In contrast, methane flames display a more uniform fuel distribution along the flame front, resulting in a less pronounced correlation between curvatures and gradients. This behavior aligns with the near-unity effective Lewis number of methane, which dampens the effects of differential diffusion, thereby leading to a more homogeneous flame front.

Upon transitioning from Condition B to the more turbulent Condition A, the correlation coefficients for hydrogen flames decrease, particularly in the later stages of combustion. Conversely, the correlation coefficients for methane flames increase under Condition A. The shift in correlation coefficients to the right from A20 to A60 for both hydrogen and methane flames at both OCs reflects an increasing positive correlation. This trend is more noticeable for hydrogen flames under Condition B, where lower turbulence levels allow differential diffusion effects to be clearer observed. However, in the later stages of flame propagation, a slight decrease or

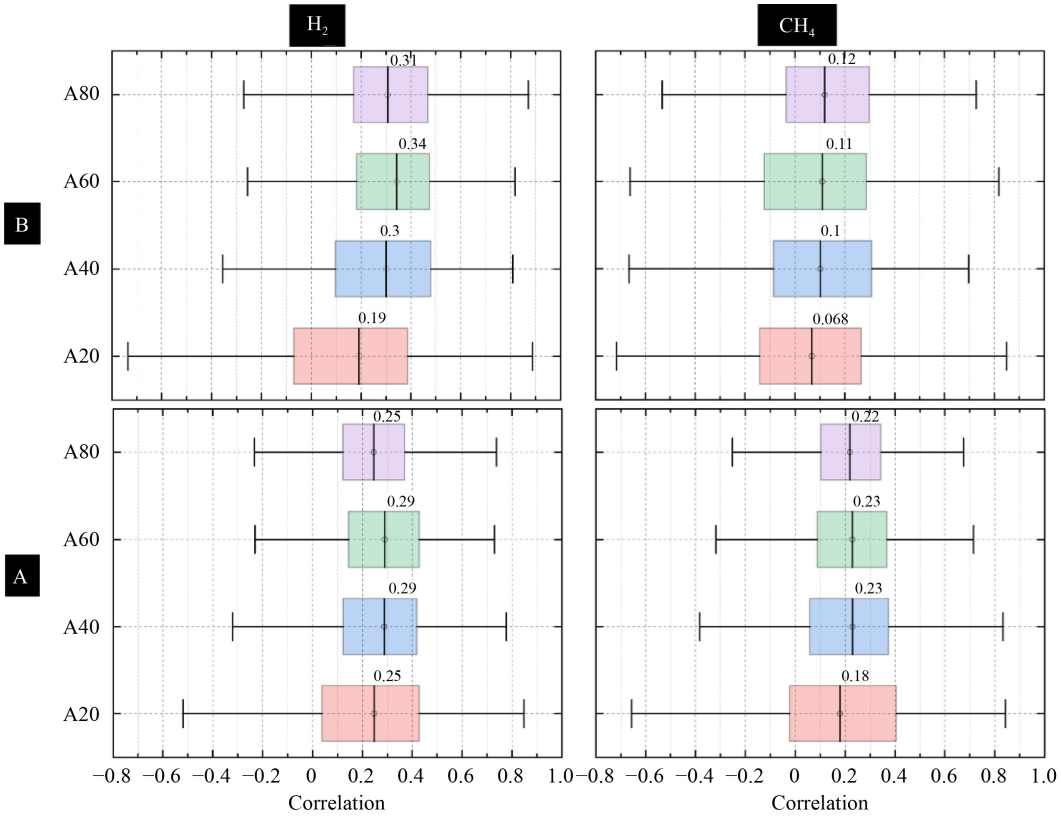

Fig. 8 Distributions of correlations between flame curvatures and gradients for hydrogen and methane flames under Conditions B and A, respectively.

stabilization in correlation coefficients is observed for both hydrogen and methane flames. This phenomenon may be attributed to the wall effect, as the flame leading edges approach the cylinder wall or piston top. This interaction leads to a reduction in flame wrinkling, which agrees with the observations of Johe et al. [37].

3.3 Flame tortuosity

The quantification of flame tortuosity, as illustrated in Fig. 9, is crucial for characterizing the complexity of flame front propagation. This parameter serves as a metric for the sinuosity of the flame, reflecting the degree to which the flame front deviates from a planar configuration. A comparative analysis of flame tortuosity across varying combustion phases for H_2 and CH_4 flames elucidates the distinct behaviors influenced by their respective thermo-physical properties and the ambient combustion conditions.

Under Condition B, H_2 flames exhibit higher mean tortuosity compared to CH_4 flames across the investigated combustion phases. As the combustion progresses from A20 to A80, the mean tortuosity of H_2 flames approximately doubled, increasing from 67.8×10^{-6} to 125.0×10^{-6}, suggesting that the flame fronts become more convoluted. In contrast, the mean tortuosity of CH_4 flames remains relatively low. Moreover, the tortuosity distributions for H_2 flames exhibit greater variation compared to CH_4 flames across different combustion cycles, indicating the higher dynamic behavior of H_2 early flames due to their pronounced thermo-diffusive instability.

When transitioning to the higher turbulence Condition A, CH_4 flames exhibit a 72% increase in mean tortuosity compared to Condition B (Fig. 9), which is a steeper rise than observed for the H_2 flames (58%). This disparity highlights the decreasing influence of thermo-diffusive instabilities on the flame wrinkling of the hydrogen flame with increasing turbulence. The increase in tortuosity is consistent with the higher flame curvatures, as shown in Fig. 5.

3.4 Equivalent flame speed

The assessment of equivalent flame speeds, as illustrated in Fig. 10, provides a macroscopic view of the propagation characteristics of H_2 and CH_4 flames under varying combustion conditions. The higher speeds observed for hydrogen are in line with the intrinsic instabilities in premixed hydrogen flames reported by Berger et al. [38], who noted that the flame speed can be significantly enhanced due to the combined effects of differential diffusion and turbulence. The significant increase in equivalent flame speeds from Condition B to A underscores the pivotal role of turbulence in accelerating flame propagation. This enhancement is attributed to intensified turbulent fluctuations and increased strain rates that interact with the flame front, leading to faster consumption of the reactants and, consequently, an acceleration of the flame front.

Moreover, the higher equivalent speeds of H_2 flames, relative to CH_4 flames, under similar combustion conditions and phases, are indicative of the accelerative influence of high thermo-diffusivity on flame propagation. The lower effective Lewis number of H_2, implying a higher sensitivity to thermal and mass diffusion imbalances, results in a more reactive flame front that responds more significantly to the variations in local curvature and strain rate. This increased sensitivity enhances the local flame speed, particularly in regions of high curvature, thereby promoting a faster overall flame propagation.

Furthermore, a notable decrease in flame speeds for both H_2 and CH_4 flames was observed during the later combustion phases (A60–A80) under various conditions. This reduction is likely attributed to wall effects as the

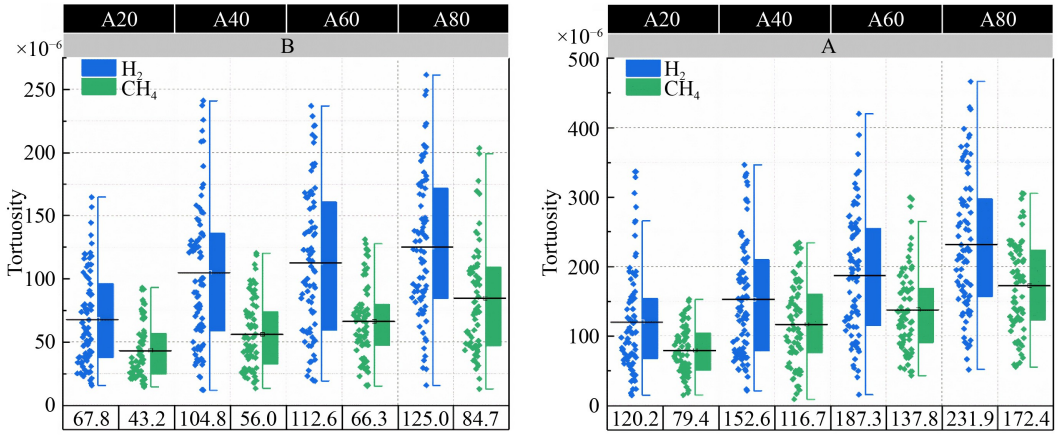

Fig. 9 Flame tortuosity distributions at different combustion phases (A20, A40, A60, A80) among all cycles (left: Condition B; right: Condition A).

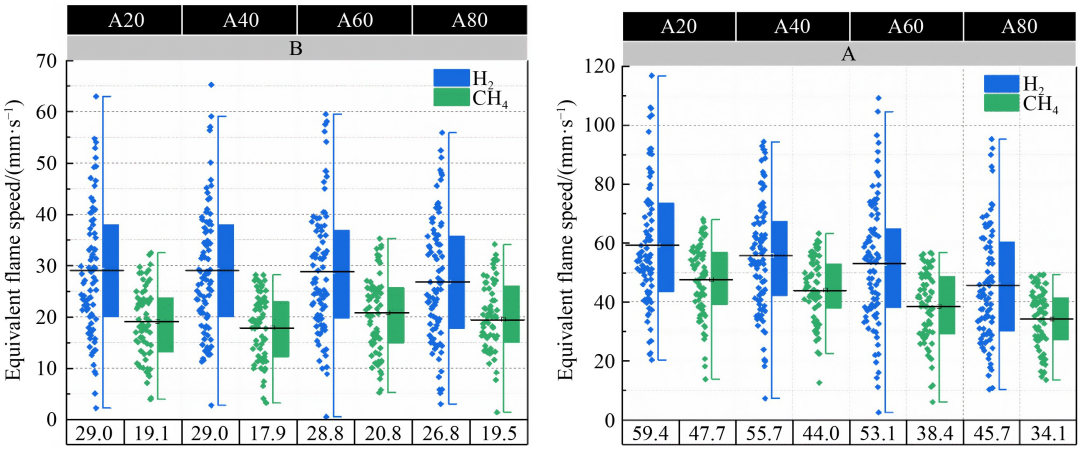

Fig. 10 Equivalent flame speed distributions at different combustion phases (A20, A40, A60, A80) among all cycles (left: Condition B; right: Condition A)

flame fronts approach the cylinder wall or piston surface.

The findings from the analysis of equivalent flame speeds are consistent with previous studies [4,8], which have established a connection between high thermo-diffusivity and accelerated flame propagation in hydrogen flames. These results further emphasize the modulating effect of turbulence on this relationship, highlighting the need to consider the interplay between differential diffusion, flame stretch, and turbulence when predicting flame speeds in practical combustion systems.

4 Conclusions

This study investigates the early flame dynamics of hydrogen-fueled spark ignition engines using optical diagnostics. High-speed planar SO_2-LIF was employed to visualize the flame front and study the topology of lean H_2 flame propagation, using stoichiometric CH_4/air mixtures as a baseline. The findings reveal that hydrogen flames, characterized by their higher thermo-diffusivity and a lower effective Lewis number, exhibit distinct behaviors in response to turbulence and differential diffusion.

Hydrogen flames show pronounced thermo-diffusive instabilities, leading to the formation of intricate flame trough/cusp structures. As turbulence increases from Condition B to A, flame wrinkling and curvature intensify, highlighting turbulence's role in modulating flame geometry. Correlation analysis indicates a strong coupling between flame curvature and gradients in hydrogen flames, particularly under low-turbulence conditions. This suggests richer fuel concentrations at the flame troughs, resulting in accelerated flame propagation.

Flame tortuosity analysis shows that hydrogen flames form more convoluted structures under low turbulence compared to methane flames, thereby enhancing surface area and reactivity. Equivalent flame speed assessment reveals higher speeds for hydrogen flames due to their thermo-diffusivity and lower Lewis number. The transition from Condition B to A increases equivalent flame speeds for both fuels, but the influence of thermo-diffusive instabilities on flame wrinkling of the hydrogen flame becomes less pronounced with increasing turbulence.

In conclusion, this study provides valuable insights into the early flame dynamics of hydrogen-fueled spark ignition engines. The results underscore the complex interplay between flame structure, curvature, flame gradients, tortuosity, and propagation characteristics, laying the groundwork for further research and optimization of hydrogen-fueled internal combustion engines.

Acknowledgements This work was supported by the Deutsche Forschungsgemeinschaft through FOR 2687 "Cyclic variations in highly optimized spark-ignition engines: experiment and simulation of a multiscale causal chain" (No. 423224402).

Competing Interests The authors declare that they have no competing interest.

References

1. Liu H, Ampah J D, Zhao Y, et al. A perspective on the overarching role of hydrogen, ammonia, and methanol carbon-neutral fuels towards net zero emission in the next three decades.

Energies, 2022, 16(1): 280
2. Çeper B A. Use of hydrogen-methane blends in internal combustion engines. In: Dragica Minic D, ed. Hydrogen Energy—Challenges and Perspectives. London: IntechOpen Limited, 2012
3. Halter F, Chauveau C, Gökalp I. Characterization of the effects of hydrogen addition in premixed methane/air flames. International Journal of Hydrogen Energy, 2007, 32(13): 2585–2592
4. Chu H, Berger L, Grenga T, et al. Effects of differential diffusion on hydrogen flame kernel development under engine conditions. Proceedings of the Combustion Institute, 2023, 39(2): 2129–2138
5. Liu H, Dankwa Ampah J, Afrane S, et al. Potential benefits and trade-offs associated with hydrogen transition under diverse carbon dioxide removal strategies. Science Bulletin, 2024, 69(1): 34–39
6. Schefer R W, White C, Keller J. Lean hydrogen combustion. In: Dunn-Rankin D, ed. Lean Combustion. Elsevier, 2008
7. Boretti A. Phased transition from methane to hydrogen in internal combustion engines: utilizing hythane and direct injection jet ignition for enhanced efficiency and reduced emissions. International Journal of Hydrogen Energy, 2024, 80: 1255–1265
8. Berger L, Kleinheinz K, Attili A, et al. Characteristic patterns of thermodiffusively unstable premixed lean hydrogen flames. Proceedings of the Combustion Institute, 2019, 37(2): 1879–1886
9. Berger L, Attili A, Pitsch H. Synergistic interactions of thermodiffusive instabilities and turbulence in lean hydrogen flames. Combustion and Flame, 2022, 244: 112254
10. Law C K. Combustion Physics. Cambridge: Cambridge University Press, 2010
11. Minamoto Y, Yenerdag B, Tanahashi M. Morphology and structure of hydrogen–air turbulent premixed flames. Combustion and Flame, 2018, 192: 369–383
12. Smallwood G J, Deschamps B M. Flame surface density measurements with PLIF in an SI engine. SAE Transactions, 1996, 2307–2317
13. Haibel M, Mayinger F. The effect of turbulent structures on the development of mixing and combustion processes in sub-and supersonic H_2 flames. International Journal of Heat and Mass Transfer, 1994, 37: 241–253
14. Wu M S, Kwon S, Driscoll J F, et al. Preferential diffusion effects on the surface structure of turbulent premixed hydrogen/air flames. Combustion Science and Technology, 1991, 78(1-3): 69–96
15. Salazar V, Kaiser S. Influence of the flow field on flame propagation in a hydrogen-fueled internal combustion engine. SAE International Journal of Engines, 2011, 4(2): 2376–2394
16. Aleiferis P G, Rosati M F. Flame chemiluminescence and OH LIF imaging in a hydrogen-fuelled spark-ignition engine. International Journal of Hydrogen Energy, 2012, 37(2): 1797–1812
17. Peñaranda A, Martinez Boggio S D, et al. Characterization of flame front propagation during early and late combustion for methane-hydrogen fueling of an optically accessible SI engine. International Journal of Hydrogen Energy, 2018, 43(52): 23538–23557
18. Fukui K, Fujikawa T, Tohyama M, et al. Laser diagnosis using optically accessible single cylinder engine. R&D Review of Toyota CRDL, 2016, 47: 1–11
19. Honza R, Ding C P, Dreizler A, et al. Flame imaging using planar laser induced fluorescence of sulfur dioxide. Applied Physics. B, Lasers and Optics, 2017, 123(9): 246.1–246.6
20. Baum E, Peterson B, Böhm B, et al. On the validation of LES applied to internal combustion engine flows: Part 1: Comprehensive experimental database. Flow, Turbulence and Combustion, 2014, 92(1-2): 269–297
21. Welch C, Erhard J, Shi H, et al. An experimental investigation of lean hydrogen flame instabilities in spark-ignition engines. Proceedings of the Combustion Institute, 2024, 40(1–4): 105391
22. Bürkle S, Biondo L, Ding C P, et al. In-cylinder temperature measurements in a motored IC engine using TDLAS. Flow, Turbulence and Combustion, 2018, 101(1): 139–159
23. Renaud A, Ding C P, Jakirlic S, et al. Experimental characterization of the velocity boundary layer in a motored IC engine. International Journal of Heat and Fluid Flow, 2018, 71: 366–377
24. Gashi S, Hult J, Jenkins K W, et al. Curvature and wrinkling of premixed flame kernels—Comparisons of OH PLIF and DNS data. Proceedings of the Combustion Institute, 2005, 30(1): 809–817
25. Shi S, Breicher A, Schultheis R, et al. Structures of laminar lean premixed H_2/CH_4/air polyhedral flames: Effects of flow velocity, H_2 content and equivalence ratio. Flow, Turbulence and Combustion, 2024, 113: 1081–1110
26. Chaib O, Hochgreb S, Boxx I. An experimental marker of thermo-diffusive instability in hydrogen-enriched flames. Proceedings of the Combustion Institute, 2024, 40(1–4): 105763
27. Grisan E, Foracchia M, Ruggeri A. A novel method for the automatic grading of retinal vessel tortuosity. IEEE Transactions on Medical Imaging, 2008, 27(3): 310–319
28. Shi S, Schultheis R, Barlow R S, et al. Internal flame structures of thermo-diffusive lean premixed H_2/air flames with increasing turbulence. Proceedings of the Combustion Institute, 2024, 40(1–4): 105225
29. Foucher F, Burnel S, Mounaïm-Rousselle C, et al. Flame wall interaction: effect of stretch. Experimental Thermal and Fluid Science, 2003, 27(4): 431–437
30. Joulin G, Mitani T. Linear stability analysis of two-reactant flames. Combustion and Flame, 1981, 40: 235–246
31. Berger L, Grinberg M, Jürgens B, et al. Flame fingers and interactions of hydrodynamic and thermodiffusive instabilities in laminar lean hydrogen flames. Proceedings of the Combustion Institute, 2023, 39(2): 1525–1534
32. Cheikhravat H, Yahyaoui M, Barret A, et al. Influence of hydrogen distribution on flame propagation. 21st ICDERS, Poitiers, France 2007
33. Smith G P, Golden D M, Frenklach M, et al. GRI-Mech 3.0. 2024–12-21, available at the website of University of California, Berkeley
34. Ji C, Wang D, Yang J, et al. A comprehensive study of light hydrocarbon mechanisms performance in predicting methane/hydrogen/air laminar burning velocities. International Journal of Hydrogen Energy, 2017, 42(27): 17260–17274

35. Khan A R, Ravi M R, Ray A. Experimental and chemical kinetic studies of the effect of H_2 enrichment on the laminar burning velocity and flame stability of various multicomponent natural gas blends. International Journal of Hydrogen Energy, 2019, 44(2): 1192–1212
36. Day M, Tachibana S, Bell J, et al. A combined computational and experimental characterization of lean premixed turbulent low swirl laboratory flames II. Hydrogen flames. Combustion and Flame, 2015, 162(5): 2148–2165
37. Johe P, Zentgraf F, Greifenstein M, et al. Laser-based investigation of flame surface density and mean reaction rate during flame-wall interaction at elevated pressure. Proceedings of the Combustion Institute, 2023, 39(2): 2159–2168
38. Berger L, Attili A, Pitsch H. Intrinsic instabilities in premixed hydrogen flames: Parametric variation of pressure, equivalence ratio, and temperature. Part 2–Non-linear regime and flame speed enhancement.. Combustion and Flame, 2022, 240: 111936